# Towards optical trapping and enantioselectivity of single biomolecules by interference of collective plasmons

RINA H. BUSTAMANTE, 1,†\* HIPÓLITO A. ARREDONDO CHAMPI, 1,2,†
DANIEL R. CORNEJO, 2,† JOSÉ ROBERTO CASTILHO PIQUEIRA, 3,† AND WALTER J. SALCEDO 1,†

**Abstract:** From the point of view of classical electrodynamics, nano-optical and enantioselective tweezers for single biomolecules have been routinely investigated using achiral and chiral localized surface plasmons, respectively. In this work, we propose the use of interference of collective plasmons (Fano-type plasmon) that exist in densely hexagonal plasmonic oligomers to design a high-efficiency nano-optical tweezer to trap individual biomolecules with a radius of 2 nm. For this purpose, we fabricated and simulated 2D hexagonal arrays of Au nanoparticles (AuNPs) with sub-wavelength lattice spacing which support collective plasmons by near-field coupling. Our full-field simulations show that densely hexagonal plasmonic oligomers can enhance the Fano-like resonances arising from the interference of superradiant and subradiant modes. This interference of collective plasmons results in a strong intensification and localization of the electric near-field in the interstice of the AuNPs. The methodology can also be extended to collective chiral near-fields for all-optical enantioseparation of chiral biomolecules with a small chirality parameter (±0.001) with the hypothesis of the existence of strong magnetic near-fields.

© 2023 Optica Publishing Group under the terms of the Optica Open Access Publishing Agreement

#### Introduction

Optical trapping of dielectric micro- and nanoparticles using only a highly focused laser beam was proposed by A. Ashkin and collaborators in the 1980s [1]. This optical tool applied to health science was very successful, especially in molecular biology to trap viruses and bacteria [2], transport organelles along microtubules [3], and displacing simple DNA molecules in viscous flow [4] as well as measuring forces associated with DNA transcription and replication [5,6]. Since 2012, many research groups have been extending the functionalities of this scientific instrument by creating, for example, various capture configurations [7,8] and adding other spectroscopic (and nanoscopic) techniques to analyze conformational changes in various macromolecules [9–11]. This integration led to the physical-chemical characterization of isolated biological micro- and nanoparticles using a low-power laser beam. However, when attempting to capture nanoparticles (< 10 nm), the gradient force was generally insufficient to overcome the destabilizing effect of the scattering force and Brownian motion. In this sense, it was understood that the local stability of an optical tweezer (OT) is strictly limited by the diffraction of classical optics. To overcome this drawback, very significant advances in nano-optics have made it possible to design OTs driven by near-fields (nano-optical tweezers, NOTs), which overcome the diffraction limit. The

<sup>&</sup>lt;sup>1</sup>Electronic Systems Engineering Department, Polytechnic School of the University of São Paulo, 05508-900 São Paulo, SP, Brazil

<sup>&</sup>lt;sup>2</sup>Department of Physics of Materials and Mechanics, Institute of Physics of the University of São Paulo, 05508-090 São Paulo, SP, Brazil

<sup>&</sup>lt;sup>3</sup>Telecommunication and Control Engineering Department, Polytechnic School of the University of São Paulo, 05508-900, São Paulo SP, Brazil

<sup>&</sup>lt;sup>†</sup>The authors contributed equally to this work.

<sup>\*</sup>rinahb@usp.br

first theoretical conception of a NOT using localized surface plasmons (LSPs) was reported independently by Novotny and Martin [12,13]. These researchers constructed an unconventional optical trapping scheme for dielectric nanoparticles (5 nm radius) using evanescent fields generated in the vicinity of an Au nanotip when light shines on it. After this proposal for nanoplasmonic optical trapping, many other theoretical and experimental works (trapping of sub-30-nm particles) were developed replacing metallic nanotips with more complex plasmonic nanostructures [14–19]. The first realization of an optical trap (plasmonic double-nanohole) for a single molecule (BSA, Bovine Serum Albumin) was carried out in 2012 with the experimental work of Pang and Gordon [20]. Also in that year, coaxial plasmonic apertures were proposed as NOTs for sub-10-nm particles [21]. In 2018, it was theoretically demonstrated that asymmetric plasmonic bowtie nanoantennas can trap nanoparticles up to 10 nm using a Fano interference process between dipolar and quadrupole modes [22]. Hong et al. (2020) fabricated an opto-thermo-electrohydrodynamic tweezer (conceived as a 2D array of plasmonic nanoholes interacting with light and an electric field) to capture and manipulate sub-10 nm particles and BSA biomolecules [23]. In that same year, many works were reported on the trapping of small particles with sizes up to 1 nm [24–28]. To achieve this feat of trapping such small objects, unconventional trap configurations were used, such as the nanoplasmonic tweezer composed of a silver-coated fiber tip and a gold film [24], strongly coupled plasmonic nanotips [25], a tip-enhanced Raman spectroscopy system [26] and graphene's Dirac plasmon in graphene nanoribbon driven by external source [27,28]. Very recently, other technologies (organic semiconductors, spectroscopic techniques and strongly coupled systems) were implemented to overcome the limitations of plasmonic systems [29–33]. In this sense, capture mechanisms in NOTs based on complex nanostructures are being investigated to improve the efficiency of optical trapping. On the other hand, biomolecules are molecules that make up living organisms. Many of them such as amino acids, sugars, and nucleotides are inherently chiral. The concept of chirality is used to distinguish molecules that cannot be superimposed, but are symmetrical with respect to a plane. While one of the enantiomers forms an effective medicine, the other can cause serious side effects [34]. Therefore, studying and designing passive processes to separate enantiomers as opposed to chemical methods (chiral chromatographic methods and electrophoresis capillary) [35] would be an essential task for the development of new products pharmaceuticals, agrochemicals, and food additives. It is known that the figure of merit of an enantioselective process (using electromagnetic fields) is the chiral dissymetry factor [36]. The definition provided by classical electrodynamics includes chirality properties in electromagnetic fields [37]. The generation and manipulation of chiral electromagnetic fields are possible in principle due to the interaction between light and carefully designed meta-structures [38–43]. The chiral optical properties can be modulated by the incident light, geometry, and material type of the meta-structure [44–46]. Optical enantioseparation of chiral nanoparticles has been achieved using symmetric nanostructures such as coaxial plasmonic apertures [44], nanoplasmonic triangle trimmers [45], and subwavelength slot waveguides [46]. On the other hand, the use of asymmetric nanostructures and nanoapertures made it possible to intensify the optical chirality and thus improve the efficiency of enantioselective trapping for sub-10 nm particles and globular chiral macromolecules [47–50]. Recently, other approaches have also been proposed in order to detect [51] and sort chiral specimens [52]. Even considering the chiral spatial structure inside the molecules to analyze its effect on the enantioselective force [53,54]. However, chiral plasmonic tweezers for efficient optical capture and enantioseparation of individual biomolecules with small chirality parameters still remain challenging. In this context, we propose (theoretically) to use of highly dense plasmonic oligomers that support Fano-type plasmons (collective plasmon interference) to design a high-efficiency nanoplasmonic tweezer based on experimental transmission measurements. The engineered nanodevice that can trap individual biomolecules of up to 2 nm radius (with linearly polarized light) can also passively sort chiral spherical biomolecules with small chirality parameters by changing the light to circularly

polarized. The hypothesis made for the latter case is that the hexagonal plasmonic oligomer supports localized magnetic plasmons.

#### 2. Methods

#### 2.1. Electrochemical nanofabrication

First, square pieces of Al (99.9995% purity, Plutatonic ALFA ZEAZAR) with a nominal thickness of  $0.035\pm0.007$  mm were sequentially cleaned in trichloroethylene, acetone, and isopropanol for 10 min each. Immediately, the Al foils (2 cm x 2 cm) were thermally annealed at 500 °C in N<sub>2</sub> for 3 hours and then electropolished (see Supplement 1, Fig. S1a-c). Self-ordered alumina nanostructures (1  $\mu$ m thick) grown on the Al surface were obtained by a two-step anodization procedure [55,56] using a simple electrochemical cell with two electrodes in 0.5 M H<sub>2</sub>C<sub>2</sub>O<sub>2</sub> at 25 °C and 45 V (see Supplement 1, Fig. S1d-i). After anodization, the synthesis of AuNPs inside hexagonal alumina nanopores was carried out by AC electrodeposition of metals [57–59]. This process was conducted in an electrolyte containing 1g/L HAuCl<sub>4</sub>·3H<sub>2</sub>O + 30 g/L H<sub>3</sub>BO<sub>3</sub>, with a pH of 1.5, AC voltage of 10 V (RMS) and a frequency of 200 Hz. In this case it was not necessary to stir the electrolyte solution. Then, the remaining Al on the backside of the nanostructured composite films (Al<sub>2</sub>O<sub>3</sub>@AuNPs) was chemically removed by immersion in a saturated CuSO<sub>4</sub>·3H<sub>2</sub>O solution by adding 3 ml of HCl (37%). Therefore, the as-obtained Al<sub>2</sub>O<sub>3</sub>@AuNPs films, suspended in water, were transferred intact to SiO<sub>2</sub> substrates.

#### 2.2. Morphology and structural characterization

The surface and cross-section of the nanostructured films on Al substrate (Al@Al<sub>2</sub>O<sub>3</sub>@AuNPs) were characterized by scanning electron microscopy (SEM) and energy dispersive X–ray spectroscopy (EDS) using a FEI Quanta 450 FEG. X-ray diffraction (XRD) of the nanostructured films on SiO<sub>2</sub> substrate (SiO<sub>2</sub>@Al<sub>2</sub>O<sub>3</sub>@AuNPs) were recorded in a Bruker diffractometer (D8-Discover) by using Cu K $\alpha$  radiation ( $\lambda$  = 1.5418A) anode operating at 40 kV and 30 mA. XRD measurements were recorded using 2 $\theta$  steps of 0.1°, 2 $\theta$  range of 30° to 110° and the counting time for XRD analysis was 2s step<sup>-1</sup>.

# 2.3. Transmittance measurements

The  $SiO_2@Al_2O_3@AuNPs$  films were optically characterized using a UV-Vis Spectrophotometer (Shimadzu UV-2600) in transmittance mode. The incidence of light (unpolarized) was normal to the plane of the AuNPs, wavelength from 300 to 800 nm, slit width 0.5 and accumulation time 1s. For transmittance measurements of the nanostructured films in a water environment, we had to transfer the  $Al_2O_3@AuNPs$  film to a quartz cuvette (handmade) with optical path length of 1mm.

#### 2.4. FDTD simulations

Electromagnetic modeling of the nanoplasmonic systems was performed using the commercial software FDTD Solutions 8.5 (Lumerical Inc., Canada). Gold nanoparticle clusters (hexagonal hexamers and heptamers) were used in the simulations. In the computational domain, linearly polarized (LP) and circularly polarized (CP) light was injected from bottom to top in the Z axis. In the boundary conditions, seven perfectly matched layers were used in the Z direction to avoid the reflection process. The dielectric constants of Au and  $SiO_2$  substrate were obtained directly using the software database. The effective refractive index of the porous alumina nanostructure (in air and water) was obtained from the effective medium theory [60]. The mesh used in all simulations was 1.5 nm. The left (right) CP light was generated using two beams of overlapping LP light with a phase difference of  $\pi/2$  ( $-\pi/2$ ). In the computational simulations, geometric parameters obtained directly from SEM micrographs and transmittance measurements were used.

#### 3. Results and discussion

#### 3.1. Nanostructured films on Al and SiO<sub>2</sub> substrates

Figure 1(a) shows a photograph of a square Al foil (L=2 cm) with electrodeposited material (circular region with an effective area of 1 cm<sup>2</sup>). Due to the reddish color in the circular region, it is possible to affirm that the AuNPs were uniformly deposited without any agglomeration. The SEM micrograph in Fig. 1(b) clearly shows the hexagonal nanostructure of nanopores and confirms their partial filling. Note that, due to the initial anodization conditions (see methods), the geometric parameters of this hexagonal alumina nanostructure are: interpore distance (w) of 110 nm, average diameter (d) of 90 nm, and thickness (h) of 1  $\mu$ m. Thus, the nanostructured composite film Al<sub>2</sub>O<sub>3</sub>@AuNPs on Al was prepared, where Al<sub>2</sub>O<sub>3</sub> represents aluminum oxide (or alumina with refractive index of 1.67) and AuNPs denote the gold nanoparticles. On the other hand, Fig. 1(c) shows the chronoamperometric curves (current densities *versus* time) of the Au electrodeposition process for three samples G1, G2, and G3, corresponding to deposition times of 60 s, 240 s, and 480 s. Note that these potentiostatic curves reveal that the electrocrystallization kinetics of AuNPs follow an instantaneous nucleation mechanism followed by diffusion-controlled growth [61,62].

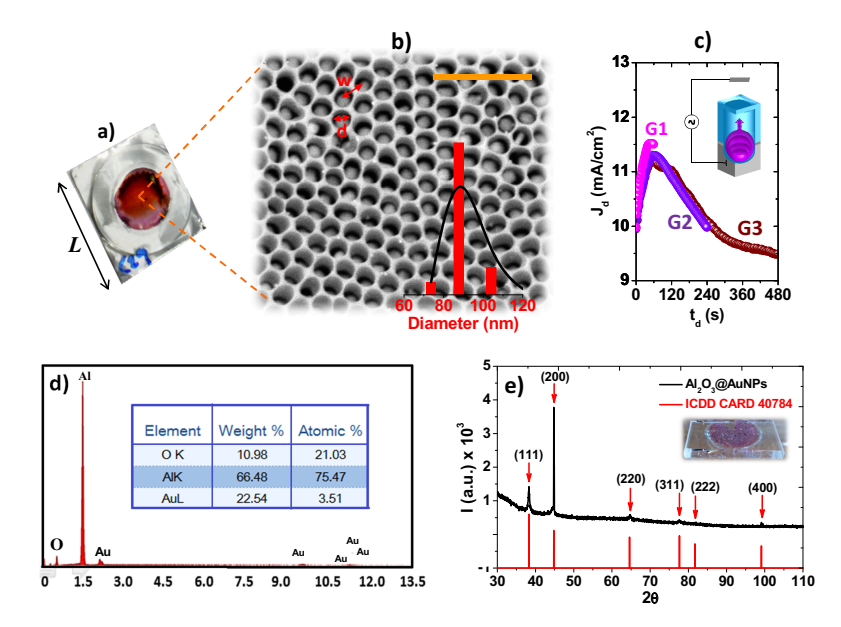


**Fig. 1.** (a) Photograph of a real sample with electrodeposited AuNPs. (b) SEM micrograph of hexagonal nanopores partially filled with Au. The inset of this panel shows the histogram of nanopore diameter distribution. The yellow scale bar is 500 nm. (c) Current densities *versus* deposition time  $(t_d)$  for three samples G1, G2 and G3 with  $t_d = 60$ , 240 and 480 s, respectively. (d) EDS analysis of the Al@Al<sub>2</sub>O<sub>3</sub>@AuNPs film. (e) XRD of the SiO<sub>2</sub>@Al<sub>2</sub>O<sub>3</sub>@AuNPs film. The standard reference ICDD card. 40784 for Au is also shown (red vertical lines).

The chemical (EDS) and structural (XRD) characterization of the AuNPs within the nanoporous are shown in Figs. 1(d) and 1(e), respectively. EDS analysis of the Al@Al<sub>2</sub>O<sub>3</sub>@AuNPs film reveals the chemical composition of the materials present with their respective percentages: Oxygen (10.98%), Al (66.48%) and Au (22.54%). Also, XRD analysis of the SiO<sub>2</sub>@Al<sub>2</sub>O<sub>3</sub>@AuNPs film reveals the crystallinity of the AuNPs. The emergence of six peaks (red arrows in Fig. 1(e)) located at  $2\theta = 38.2^{\circ}$ ,  $44.7^{\circ}$ ,  $64.7^{\circ}$ ,  $77.6^{\circ}$ ,  $81.7^{\circ}$  and  $99.1^{\circ}$  correspond, respectively, to the crystallographic planes (111), (200), (220), (311), (222) and (400) of a face-centered cubic

(FCC) structure for Au, with preferred growth direction in the (200) plane. The appearance of these peaks in the X-Ray diffractogram is in perfect agreement with the standard ICDD Card No. 40784 for Au (vertical red lines in Fig. 1(e)).

#### 3.2. Transmittance spectra for nanostructured films with sub-wavelength lattice spacing

Figure 2 shows the experimental (panel 2a-c) and simulated (panel 2d-f) normalized transmittance spectra for three different hexagonal arrangements of AuNPs in air (dashed lines) and water (continuous lines) environments. Each of the AuNPs arrays corresponds to the previously defined G1, G2 and G3 samples with lattice spacing of 50 nm, 30 nm and 20 nm, respectively. It is worth mentioning that each of these transmittance curves represents a statistical average of several measurements carried out on the nanostructured films (see Supplement 1, Fig. S2). It is clear to observe in G1 the formation of spherical AuNPs with an average diameter of 60 nm (SEM image in panel 2a). In sample G2, there is formation of almost spherical AuNPs with an average diameter of 80 nm (SEM image in panel 2b), and sample G3 revealed the formation of slightly elongated spherical AuNPs with an average diameter of 90 nm (SEM image in panel 2c). Yellow scale bars in all SEM images, 100 nm. Photographs of SiO<sub>2</sub>@Al<sub>2</sub>O<sub>3</sub>@AuNPs nanostructured films are shown in the inset in panel 2a-c labeled by G1, G2 and G3.

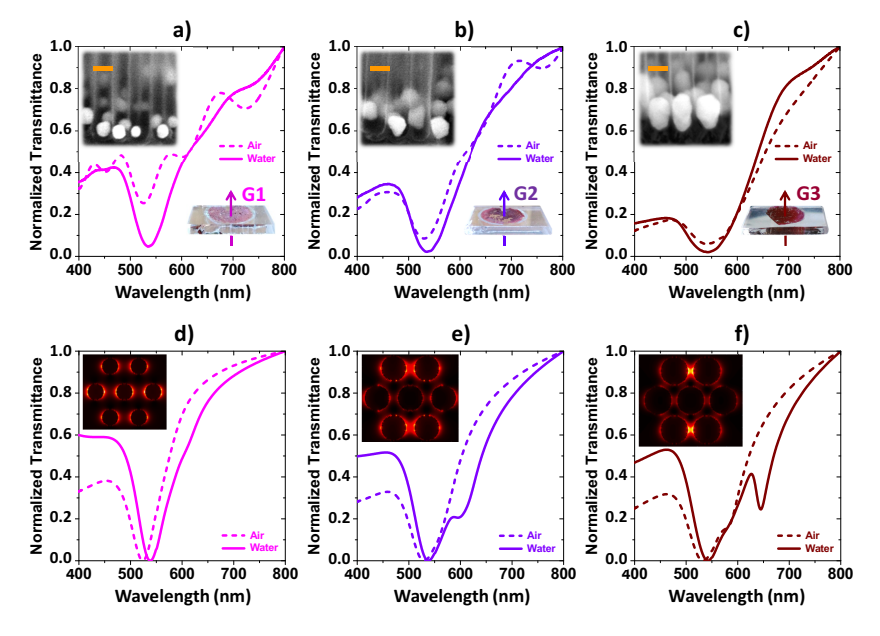


**Fig. 2.** Experimental (a-c) and simulated (d-f) normalized transmittance for three different hexagonal arrangements of AuNPs in air (dashed lines) and water (solid lines) environments. Top-left panel: (a-c) SEM images (front view) and (d-f) hexagonal heptamers (top view) of AuNPs are shown, respectively. Lower right panel: (a-c) photographs of the  $SiO_2@Al_2O_3@AuNPs$  films, labeled by G1, G2 and G3.

Although the AuNPs did not appear perfectly spherical, a sphere approximation can be made without loss of generality, since we are interested in their collective behavior. With this, the problem can be minimized so that the simulations fit well with the experimental data. Regarding the transmittance simulations (panel 2d-f), 2D hexagonal heptamers (plasmonic oligomers) with different packing factors, 27, 48, and 61%, corresponding to lattice spacings 50, 30, and 20 nm were used. Transmittance spectra were obtained under unpolarized (experiment) and polarized (simulation) light. In the latter case, the electric field was parallel to a linear chain of AuNPs,

normal to the plane of the AuNPs. The most important feature in the simulated and experimental transmission spectra is the existence of well-defined bands (minima in the transmission spectra) where the light drastically attenuates. These spectral positions (symmetric dips), coincide exactly. It is in these bands where the AuNPs absorb the greatest amount of energy from the incident light wave due to the plasmonic resonance of the AuNPs [63]. Although the experimental and simulated curves do not fit exactly across the entire spectral range, due to imperfections in the fabrication process and the finite number of AuNPs, the spectral position and broadening of these plasmonic modes follow an increasing trend as the lattice spacing decreases. In this context, the G2 and G3 nanostructured films (fabricated and simulated) capture the two main features of the plasmonic lattice resonances by near-field coupling (or collective plasmon resonances) [64]: redshift and broadening of the plasmonic resonance. The upper left part of Fig. 2(d-f) shows the distributions of electric near-field intensity in the collective plasmonic resonances for each of the plasmonic oligomers corresponding to their lattice spacing. Maximum near-field intensities (hot spots) occur when AuNPs are immersed in water with  $\lambda_r = 535$  nm (panel 2d), 539 nm (panel 2e), and 545 nm (panel 2f) whose field intensification factor ( $f_E = |\mathbf{E}|^2/|\mathbf{E}_o|^2$ ) are 23, 33 and 81, respectively. In this context, we see that there are simultaneous spectral changes in both the far-field (symmetric drops in the transmission spectrum) and the near-field (distribution and intensification) as the lattice spacing decreases (AuNPs closer together). This means that there is an interaction between AuNPs due to the overlap of their near fields. Similar results were recently obtained by R. Borah et al. [65] for hexagonal arrays of Ag and Au nanoparticles with diameters of approximately 20 nm. The ripples in the transmission spectra for the case of AuNPs arrays in air environment (dashed lines) are due to the presence of the alumina nanostructure since the material contrast between air and alumina is approximately 1.7. In the case of AuNPs arrays in water, this contrast drops to 1.3, which results in smoother curves.

Simplified modeling of the collective (plasmonic) interaction process that takes place in samples G1, G2, and G3 can be extracted from the intensity distribution of the near fields (inset of Fig. 2(d-f)). For example, for G1 film, the electromagnetic modeling that predicts its transmittance spectrum is that of a simple AuNP (see Supplement 1, Fig. S3a) since the AuNPs in the oligomer interact weakly. The modeling for the G2 film is that of a dimer, since in this approach a pair of AuNPs begin to interact and their transmission spectrum fits well with the experimental data (see Supplement 1, Fig. S3b). Similarly, for the G3 film (smallest lattice spacing, 20 nm), the interaction of three collinear AuNPs to the incident electric field is enhanced and its transmission spectrum also fits well with the experimental data (see Supplement 1, Fig. S3c). Note that these simplified models capture the effects of spectral shift and increase in plasmonic bandwidth in agreement with experimentally observed spectral changes. The near-field intensity distributions (see Supplement 1, inset of Fig. S3d-f) and their corresponding intensification factors ( $f_E$ ) reveal how the near-field is intensified at  $\lambda_r = 550+6\Delta$  nm (with  $\Delta$ =0,1,2) and located in the spacing between AuNPs. The maximum value reached was for the linear trimer ( $f_E \approx 250$ ) which is five times greater than for a plasmonic monomer. Furthermore, due to the linear polarization of light (electric field parallel to the axis that joins the AuNPs) the near field (hot spot) is concentrated on the axis that joins the nanoparticles. Thus, the minima in the transmission spectrum (and its spectral changes) of samples G2 and G3 (relative to G1) can be explained by the dipole-dipole coupling model [66].

Figure 3 shows, quantitatively, the effect of the lattice spacing of the AuNPs arrays on the position of the plasmon resonance wavelength ( $\lambda_r$ , panels 3a,b) and on the full width at half minimum (FWHM) of the curve transmission (panels 3c,d). From Fig. 3(a), it can be clearly observed that  $\lambda_r$  increases exponentially (redshift) as the lattice spacing decreases. In this case, the numerical simulations (red circles) are in agreement with the experimental data (blue triangles). For comparison purposes,  $\lambda_r$  was also plotted for an isolated AuNP (orange squares) for both air (panel 3a) and water (panel 3b) environments. The redshift of the plasmon resonance

is therefore a confirmation of the interference effect of LSPs. Similarly, the effect of increasing the size of the AuNPs (or decreasing the lattice spacing) exponentially broadens the FWHM of the plasmon (panels 3c,d) in contrast to an isolated AuNP (orange squares). As already mentioned previously, the experimental (blue triangles) and simulated data (red circles) for the FWHM differ slightly (see Fig. 3(c,d)) due to the emergence of an asymmetric dip in the transmission spectrum (see Fig. 2(c,f)). But both follow an exponential trend. In this context, it appears that the plasmon existing in a hexagonal AuNP oligomer (and also in the fabricated samples) with a lattice spacing less than 30 nm (packing factor greater than 48%) is strictly a collective plasmon. In hexagonal samples with lattice spacings greater than 30 nm (packing factors less than 48%), the lattice plasmon coincides with a LSP.

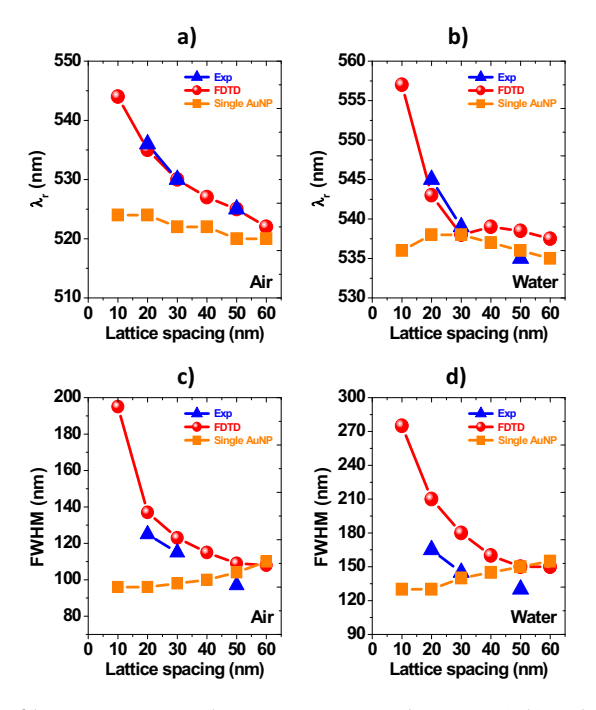


**Fig. 3.** Effect of lattice spacing on the resonance spectral position (a,b) and on the FWHM (c,d) of the plasmon for the different hexagonal arrangements of AuNPs in air (a,c) e water (b,d) environments.

A very striking feature in the simulated transmission spectra for sample G3, which has not been mentioned so far, is the appearance of a second asymmetric absorption band (second minimum in the transmission spectra of Fig. 2(f)); most prominent for the G3 hexagonal heptamer (in water) with lattice spacings of 20 nm ( $\lambda_a \approx 650$  nm). Note that an asymmetric band also appears (and is hidden) in the experimental transmission spectrum (infinite hexagonal arrangement), with only a slight inflection around 580 nm (see gray region in Fig. 4). Figure 4(a) shows ten (normalized) transmission measurements performed on sample G3 (with 20 nm lattice spacing) in contrast to the statistical average value (see Fig. 2(c)). The purpose of this set of measurements is to experimentally observe the appearance of the asymmetric band (Fig. 4(b)) revealed in the computational simulations. Note in the magnified spectrum in Fig. 4(b) (gray band) that the curves have a gradual shape (from top to bottom) with the appearance of the asymmetric plasmonic band (blue arrow). This subtle characteristic of the emergence of an asymmetric plasmonic band can be understood a priori only by considering the lattice spacing. Due to imperfections in the sample manufacturing process, the lattice spacing in the hexagonal arrangement is not a

constant parameter. This parameter is approximately between 15 and 25 nm. When we carry out transmission measurements, in a certain region of the sample, some AuNPs must have been closer than others on a nanometer scale of  $20 \pm 5$  nm (the non-sphericity of the NPs must have also contributed). Therefore, when the AuNPs are closer ( $\approx 15$  nm) the appearance of the asymmetric band will be more prominent (blue arrow) and when the AuNPs are further apart ( $\approx 25$  nm) the asymmetric band will only be a slight inflection (red arrow). In this way, the hypothesis is that the experimentally observed asymmetric plasmonic band is very sensitive to the lattice spacing. The subtlety of the asymmetric profile observed in the transmittance spectra of sample G3 (and almost imperceptible in G2), of being sensitive to the separation distance between nanoparticles (gap), inspired the study to intensify and understand the mechanism of the asymmetric drop in the transmittance spectrum.

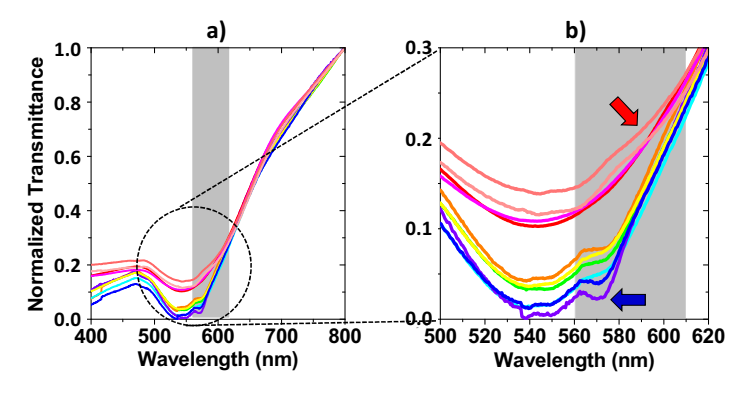


**Fig. 4.** (a) Experimental transmittance spectrum (normalized) for specimen G3 (hexagonal array of AuNPs with lattice spacing of 20 nm). (b) Magnified spectrum in the range 500-620 nm showing the emergence of the asymmetric plasmonic band (blue arrow).

# 3.3. FDTD simulations of transmittance spectra for hexagonally dense plasmonic oligomers

Figure 5(a-c) shows the simulated transmittance spectra for a plasmonic oligomer of AuNPs with lattice spacing (g) varying between 5 and 50 nm. The computational simulations were carried out in three environments with effective refractive indices n = 1 (panel 5a), n = 1.17 (panel 5b), and n = 1.33 (panel 5c). Note that n = 1.17 is the effective refractive index of the Air@Al<sub>2</sub>O<sub>3</sub> composite (air-filled nanopores). These transmission spectra show that when decreasing the lattice spacing  $(g \to 5 \text{ nm})$ , in the three environments, the appearance of asymmetric dips is more pronounced (see dashed black lines). The transition from isolated to collective plasmons is clearly visible in the transmittance spectra when decreasing the lattice spacing. Particularly, in the transmission spectra for air (Fig. 5(a)), the existence of two minima for g = 5 nm is observed. One of the minima corresponds to the collective plasmon (symmetric dip at  $\lambda_c = 575$  nm) and another corresponds to the Fano-type plasmon (asymmetric dip at  $\lambda_a = 675$  nm). When the refractive index of the host medium increases (n>1), the Fano-type plasmonic resonance for g = 5 nm (denser plasmonic oligomer) shifts to the red with sensitivity of  $S = \Delta \lambda / \Delta n \approx 500$ nm/RIU. The same idea can be applied to the Fano-type plasmon with g = 10 nm. This high sensitivity of the asymmetric profile with its surroundings is desirable to achieve a high figure of merit in refractive index sensing and in the design of single-molecule optical biosensors. For less dense plasmonic oligomers ( $g \ge 30$  nm), the optical properties of the oligomer (or infinite hexagonal arrays of AuNPs) are dictated by the interference from LSPs (collective plasmon) using dipole-dipole coupling of linear or circular chains of nanoparticles. While Fano-type plasmonic resonances are a more complex phenomenon. It is well known that, in plasmonic systems, the

Fano-type resonances are produced by the interaction between the system's modes, a superradiant mode, and a subradiant mode [67–69]. To qualitatively visualize the origin of the Fano-type plasmon, the plasmonic heptamer of AuNPs can be decomposed, imaginatively, into simpler subsystems (see Fig. 5(d)) consisting of a hexamer (circular ring of AuNPs) and a monomer (simple AuNP). Such subsystems hybridize to create two modes, the superradiant optical mode (collective plasmon in the hexamer in phase with the plasmon located in the monomer) and the subradiant optical mode (collective plasmon in the hexamer out of phase with the plasmon located in the monomer) [70]. It is these two modes that interfere destructively to produce the Fano-type plasmonic resonance observed in the transmission spectra of Fig. 5(a-c) for plasmonic oligomers with  $g \le 60n - 50$  (nm) [66,71]. Therefore, the mechanism for Fano-type plasmonic resonance is generated from the interference of collective plasmons.

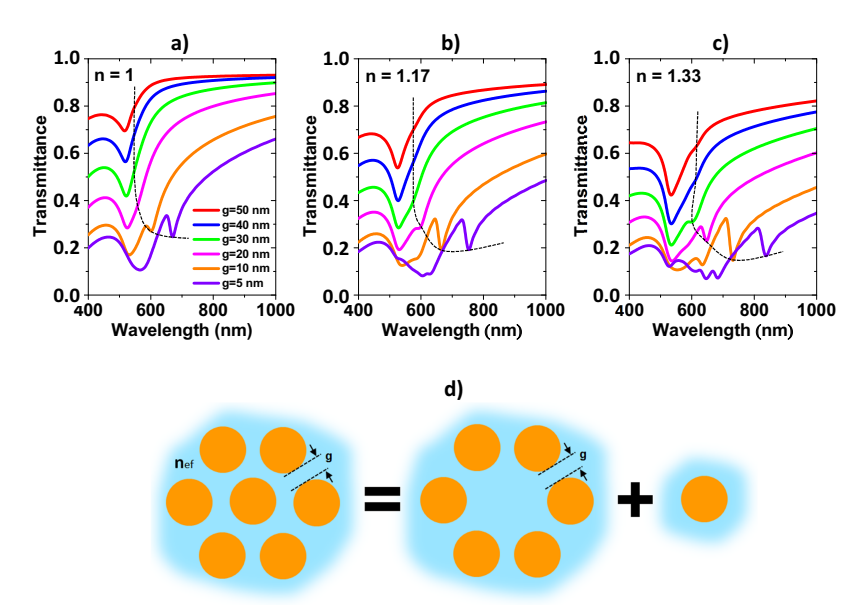


**Fig. 5.** (a-c) Simulated transmittance spectra for a plasmonic heptamer with lattice spacing (g) varying between 5 and 50 nm. The simulations were carried out in three host media with refractive indices (a) n = 1, (b) n = 1.17, and (c) n = 1.33. (d) Decomposition of the plasmonic heptamer into a hexamer (circular ring of AuNPs) and a monomer (simple AuNP). The parameter g represents the lattice spacing in the heptamer and the distance between AuNPs in the hexamer.

In order to elucidate the sensitive character of Fano resonance to the lattice spacing and asymmetry of the hexagonal oligomer, Fig. S4 of Supplement 1 shows an asymmetric plasmonic heptamer (in air) composed of a circular ring of AuNPs with diameter D=105 nm (hexamer with a distance of 5 nm between AuNPs) and a simple AuNP with diameter (d) varying between 0 and 108 nm. The parameter g, in this particular diagram, represents the distance between the central AuNP and any AuNP in the hexamer. Note that when the central AuNP of the heptamer disappears (d=0), the transmission spectrum, which corresponds to the hexamer with g=5 nm (dashed line in Fig. S4b), shows no asymmetric dip. This occurs even for heptamers with  $d \le 100$  nm (or  $g \ge 10$  nm). The asymmetric dip appears when the diameter of the central AuNP increases above 100 nm or the lattice spacing decreases below 10 nm. The asymmetric dip becomes more prominent and more sensitive to the gap between AuNPs. Furthermore, this Fano-type plasmon is further intensified due to the asymmetry of the plasmonic oligomer with d=108 nm (orange color transmittance spectrum, g=2 nm). Thus, the simple fact of nanometrically approaching

the AuNPs in a hexagonal configuration (plasmonic oligomer) induces an asymmetry in the transmission spectrum related to the Fano-type plasmonic resonance.

In Figs. 6(a-c), the electric near-field intensification factors are graphically represented as a function of the wavelength of the incident wave for a symmetric plasmonic oligomer with g=5 nm and diameters of AuNPs of 105 nm. Calculations were carried out for the three environments with n=1 (air), 1.17 (air-Al<sub>2</sub>O<sub>3</sub>) and 1.33 (water). In the three cases presented, the maximum value of the field intensification factor (labeled by 1), which is  $f_E \approx 5500$ , remains almost constant at each of the spectral positions  $\lambda_1(n)=165.8+493.6n$ . Note that these spectral positions are related to the positions of the Fano-type resonances in the plasmonic oligomer considered (g=5 nm). Knowing the sensitivity of our plasmonic system, S=494 nm/RIU, the system's figure of merit (FOM) can be found by applying the formula FOM = S/FWHM, where FWHM now it is the full width at half minimum of the Fano-type profile (see resonance profiles 1 in Fig. 6(a-c)). The FWHM for the Fano profiles is approximately 30 nm for all environments considered, thus the FOM = 17 RIU<sup>-1</sup>.

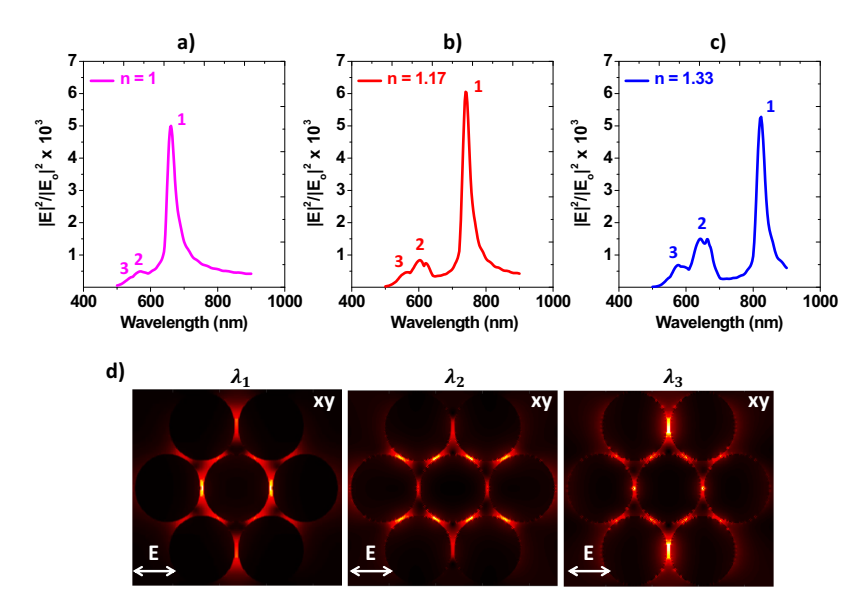


**Fig. 6.** (a-c) Near-field enhancement factors as a function of incident wave wavelength for a plasmonic oligomer with g=5 nm (D=d=105 nm). The calculations were carried out for three environments with effective refractive indexes (a) n=1, (b) n=1.17 and (c) n=1.33. (d) Near-field intensity distributions for the plasmonic heptamer (plane Z=0) corresponding to resonance wavelengths  $\lambda_1$ ,  $\lambda_2$  and  $\lambda_3$ . The heptamer is parallel to the XY plane (Z=0). The incident wave is in the Z direction and the polarization of the electric field is shown in panel (d).

The plots of near-field intensification also reveal the existence of two dipolar plasmonic modes labeled by  $\lambda_2$  and  $\lambda_3$  with intensification factors lower than 2000. According to the transmission calculations carried out independently for the plasmonic subsystems, AuNPs hexamer and simple AuNPs (see Supplement 1, Fig. S5), it is found that the emergence of the  $\lambda_2$  resonant plasmonic mode belongs to a Fano-type resonance (relatively weak compared to  $\lambda_1$ ) intrinsic to the dense plasmonic hexamer (g=5 nm). The  $\lambda_3$  plasmonic mode with the lowest enhancement factor ( $\approx 500$ ) corresponds to the collective plasmonic mode of the hexamer. Unlike the strong Fano resonance  $\lambda_1$ , the enhancement factors for the  $\lambda_2$  and  $\lambda_3$  resonances increase as the refractive index of the medium changes from n=1 to n=1.33. Furthermore, the spectral positions of these weak plasmonic modes also redshift.

Figure 6(d) shows the near-field intensity distributions (electric field) for the resonance wavelengths  $\lambda_1$ ,  $\lambda_2$  and  $\lambda_3$  (see panel 6a-c) of the aforementioned dense plasmonic oligomer. These distributions were calculated in the XY plane (Z = 0), parallel to the plane of the AuNPs. The incident wave is parallel to the Z direction and the electric field is parallel to the XY plane in the same direction of a linear chain of AuNPs. As observed in the AuNPs cluster, there are three enhanced plasmonic coupling configurations (at different wavelengths  $\lambda_i$ ) related to the three maximum electric field intensification factors. First, the Fano-type plasmon  $\lambda_1$  which originates from a strong coupling (interference) between the superradiant and subradiant collective plasmons (see Fig. 5). The presence or absence of the central AuNP activates or deactivates the formation of this Fano-type resonance. In superradiant mode, the oscillating plasmons in each monomer are in phase, exhibiting a broadening in the plasmonic band due to radiative damping. For the subradiant mode, the sum of plasmonic polarizations in the hexamer oscillates oppositely to the plasmonic polarization in the central monomer. Note that in this resonance the points of maximum intensification (hot spots) are located at the ends of the central AuNP in the same direction as the incident electric field (with  $f_E \approx 6000$ ). Second, the weakly asymmetric Fano-like plasmon ( $\lambda_2$ ) originates from the strong coupling ( $g \leq 10$  nm) of the AuNPs in the dense plasmonic hexamer. In this configuration, the hot spots (with  $f_E \approx 750$ ) are located in the gaps between the central AuNP and the hexamer (locations complementary to the Fano-type resonance  $\lambda_1$ ). Third, the collective plasmon ( $\lambda_3$ ) originates from an interference of LSPs in the hexamer. The hot spots ( $f_E \approx 250$ ) are located in the upper and lower dimer spacings of the plasmonic heptamer (locations complementary to the  $\lambda_2$  Fano-type resonance). From an experimental point of view, all interparticle regions (interstices between AuNPs) are activated with localized near-fields due to unpolarized incident light. In this sense, we show that a highly dense hexagonal plasmonic oligomer supports a high sensitivity Fano-type resonance (≈ 500 nm/RIU) in the far-field spectrum and high near-field enhancement factor ( $\approx 6000$ ). Such resonance is very sensitive to lattice spacing and arises from a collective plasmon interference mechanism.

## Optical trapping and enantioselectivity of individual biomolecules using Fano-type plasmons

Applications of Fano-type plasmonic resonance (or collective plasmon interference) existing in hexagonally dense plasmonic oligomers will be given to improve the efficiency of nano-optical and enantioselective tweezers for individual chiral molecules. Single-molecule optical trapping uses the optical interaction potential (U) between the biomolecule and the near-field created by the plasmonic oligomer. In the case of small achiral particles  $(r << \lambda)$  the quasi-static approximation can be considered due to the physical conditions of the problem. Thus, the biomolecules can be modeled phenomenologically as isotropic dielectric spheres whose interaction potential is given by

$$U = -\frac{3}{4}V\varepsilon_o n^2 \left(\frac{m^2 - 1}{m^2 + 2}\right) |\mathbf{E}|^2 \tag{1}$$

Here  $V=4/3\pi r^3$  is the volume occupied by the molecule,  $\varepsilon_o$  is the electrical permittivity of the vacuum, n is the refractive index of the environment and m is the relative refractive index of the molecule. The near-field intensity distribution  $|\mathbf{E}|^2$  was calculated using the FDTD simulations (see Fig. 6(d)). Figure 7(a) shows the optical potential of the trap in the Z=0 plane for a spherical molecule (r=2 nm) with refractive index n=1.59 (gelatinous protein) [72], immersed in an environment that can be air (n=1) or water (n=1.33). The nano-optical tweezer was designed using a hexagonal plasmonic oligomer with a lattice spacing of 5 nm (or AuNPs diameter of 105 nm). Note that the trap is very stable with  $U_{min} < -10$  kT/100mW, FWHM $_x = 3$  nm and FWHM $_y = 8$  nm (see Figs. 7(b) and 7(c)). In this case, the biomolecule has zero chirality parameter (k=0) since we are simply interested in its capture. Figure 7(b,c) shows the cross-section of the transverse trapping potential ( $U_{xy}$ ) along Y=0 and  $X=\pm52.5$  nm for two

different cases: when the particle is in air (left *Y* axis) and when the particle is in water (right *Y* axis in blue). Note that when the biomolecule is in the air, the trapping potential depth is -58.7 kT/100mW. Therefore, only 17 mW is needed to confine the molecule in the interstice of the AuNPs. When the molecule is in water, the potential depth is reduced to 39.5 kT/100mW due to the reduction in refractive index contrast between the molecule and the surrounding medium. As a result, the minimum power required to confine the molecule is increased to 25 mW.

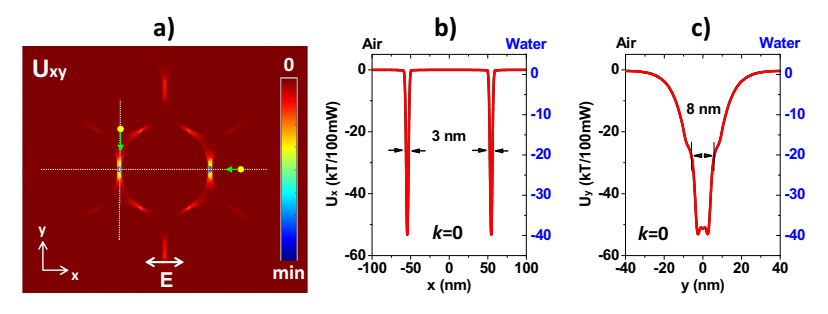


**Fig. 7.** (a) Transverse optical potential (plane Z=0). (b,c) Cross sections of the optical potential (Uxy) for a 2 nm biomolecule with refractive index (n) of 1.59 placed in air (n=1) and water (n=1.33). Cross sections were obtained along (b) Y=0 and (c) |X|=52.5 nm. The FWHM of the potential along the X and Y directions is 3 and 8 nm, respectively.

In this context, the proposed nanoplasmonic tweezer is highly efficient with the ability to trap individual biomolecules induced by the high near-field intensification factor. The interference of collective plasmons (or Fano-type resonance), the product of a "gap" of a few nanometers between AuNPs, induces a highly localized confinement of the electric field in the interstices of the AuNPs in the same direction as the incident electric field (Fig. 7(a)). In contrast to the work reported by Saleh and Dionne [21], and Hong et al. [23], the optical potential generated by the oligomer no longer acts on a thin layer of a few nm above the surface of a nanostructure. Thus, the separation efficiency was increased. One of the advantages of using symmetrical plasmonic oligomers is that these support Fano-type plasmons with high field enhancement factor and, therefore, deep optical potential for stable and efficient trapping.

Enantioselective nano-optical tweezers emerged in order to seek an optical alternative to chemistry problems to separate chiral compounds. Figure 8(a) (8(b)) shows computational simulations of the optical potential between the S (R) enantiomer and the chiral near-field (chiral Fano-type plasmon) created by a hexagonally dense plasmonic oligomer (g = 5 nm). This chiral Fano-type plasmon is induced by the interaction of a CP light with the plasmonic oligomer. The interaction potential of the S(R) enantiomer,  $U^{S,R}$ , randomly oriented and immersed in an arbitrary chiral electromagnetic field is given by [47,73]:

$$U^{S,R} = -\frac{\alpha}{4} |\mathbf{E}|^2 - \frac{\beta}{4} |\mathbf{H}|^2 + -\frac{\gamma}{2} |\mathbf{E}| |\mathbf{H}| \theta_{i\mathbf{E},\mathbf{H}}$$
 (2)

where  $\alpha$ ,  $\beta$  represent the real part of the electric and magnetic polarizabilities of the enantiomer, respectively. The quantity  $\gamma$  is the imaginary part of the chiral polarizability and its sign depends on the choice of enantiomer S(+) or R(-). The **E**, **H** fields are generic and can represent chiral near-fields (localized and collective) created by complex metallic and dielectric meta-structures. The angular variable  $\theta_{i\mathbf{E},\mathbf{H}}$  is the angle between the vectors i**E** and **H**, and measures the degree of asymmetric twist of the electromagnetic fields. Due to the symmetry of the plasmonic oligomer, the **E**, **H** fields represent enantiomorphic chiral fields [47]. With regard to enantioselectivity, the plasmonic oligomer is also capable of selecting small enantiomers (biomolecules) whose chirality parameter (numerical value) depends on the magnetic field intensification factor in

contrast to asymmetric structures that require a symmetry break in the nanostructure to improve optical chirality [47,49].

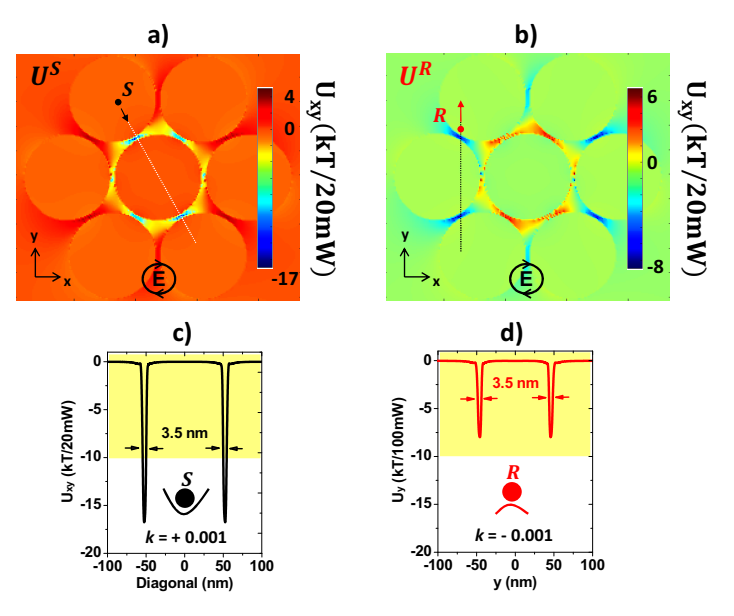


**Fig. 8.** (a,b) Enantioselective optical potentials in the Z=0 plane for the S and R enantiomers with incident LCP light. (c,d) Cross sections of the enantioselective optical potential for a 2 nm enantiomer with refractive index (n) of  $1.59 \pm 0.001$  placed in water (m = 1.33). Cross sections were obtained along the (c) diagonal and (d) |X| = 40 nm. The FWHM of the potential along the diagonal and Y axis is 3.5 nm, respectively.

For the design of an enantioselective nanoplasmonic tweezer, non-magnetic enantiomers (in water) with a radius of 2 nm and refractive index  $n_{\pm} = 1.59 \pm |k|$  will be considered, where  $k = \pm 0.001$  is the chirality parameter with S(+) and R(-). Thus,  $\alpha = 1.97 \times 10^{-37}$  m<sup>3</sup>,  $\beta = -6.94 \times 10^{-39}$  m<sup>3</sup> and  $\gamma = \pm 9.78 \times 10^{-38}$  m<sup>3</sup>, which correspond to the polarizabilities of biomolecules (protein material). Note that no dual-symmetric conditions were used. Dual-symmetric conditions were used to maximize the optical chirality [47]. Only one crucial hypothesis should be mentioned for the enantioselective nanodevice to work efficiently is that the hypothetical plasmonic oligomer, in addition to intensifying the near electric field, also intensifies the near magnetic field (existence of magnetic plasmons). This can be accomplished with SiO<sub>2</sub>-Si nanoshells, hollow Au nanocylinders, and metal-insulator-metal oligomers [74–76]. The investigation of these types of meta-structures is beyond the scope of this manuscript and only the effect of the phenomenon on the selectivity of enantiomers will be considered.

It is known that the electric near-field intensification can be defined with  $f_E = |\mathbf{E}|^2/|\mathbf{E}_o|^2$ , so it is also possible to define the magnetic near-field intensification as  $f_H = |\mathbf{H}|^2/|\mathbf{H}_o|^2$ . Plasmonic systems are generally non-magnetic so that  $f_H \approx 1$ . However, for large values of  $f_H$  it compensates for small values of  $\gamma$ . Thus, under the hypothesis that  $f_H = 5000$ , maintaining the intensification of the electric near-field as reported in Fig. 6(c) ( $\lambda_1$ ), the enantioselective trapping selects one enantiomer from the other. In other words, the S enantiomer (Fig. 8(c)) would be trapped with  $U^S < -10 \text{ kT/20mW}$ , when the incident light is LCP; however, the R enantiomer would be weakly attractive due to thermal effects (-10 kT) since  $U^R > -10 \text{ kT/20mW}$  (Fig. 8(b)). Figure 8(c) shows the cross-section of the transverse trapping chiral optical potential (S-enantiomer) along the diagonal (see dotted line in Fig. 8(a)). Note that the minimum value of the trapping potential is -17 kT/20mW with FWHM = 3.5 nm. That is, only 20 mW is needed to stably confine

the biomolecule in the diagonal interstice of the AuNPs. Regarding the R-enantiomer, the potential depth is reduced to -8 kT/20mW with the same power of the incident light. As -8 KT is lower than the minimum energy required to trap the R-enantiomer, Brownian motion causes the R-enantiomer to escape the trap. The inset of Fig. 8(c,d) shows schematic representations for the enantioselective process. While the S-enantiomer (black circle) is stably trapped in a potential well, the R-enantiomer (red circle) is free (potential barrier) from any attractive chiral force effect. Therefore, the designed enantioselective nanoplasmonic tweezers demonstrate high efficiency with the ability to select only an individual enantiomer using LCP light (see inside Figs. 6(c) and 6(d)). By changing the handedness of the incident field (RCP light) it is possible to reverse the process, that is, trap the R enantiomer, while the S enantiomer is weakly repelled.

#### 4. Conclusion

In summary, we have fabricated and simulated hexagonal arrays of AuNPs with lattice spacings smaller than 60 nm. Transmittance measurements and simulations (in air and water environments), at normal incidence, showed small plasmonic redshifts with a considerable increase in plasmonic bandwidth. Such far-field spectral changes, sensitive to lattice spacing, were attributed to nearfield coupling. A careful observation of the transmission spectrum for the hexagonal arrangement with smaller lattice spacing (20 nm) indicated that in addition to the presence of the collective plasmon, a very weak asymmetric resonance (Fano-type plasmon) emerged. Computational simulations for hexagonal plasmonic oligomers with lattice spacing less than 10 nm showed strong Fano-type resonances originating from the interference of superradiant and subradiant modes. Such interference of collective plasmons resulted in a strong intensification and localization of the electric near-field. Using these results, a high-efficiency nanoplasmonic tweezer was designed to stably trap individual molecules with a size of 2 nm. An optical enantioselectivity nanodevice was also designed for chiral molecules with a small chirality parameter ( $\pm 0.001$ ) with the hypothesis of the coexistence of electric and magnetic collective plasmons in a hypothetical plasmonic oligomer, that is, with strong enhancement of the electromagnetic near-field. From an experimental point of view, dense plasmonic oligomers could be candidates to manufacture (by advanced lithographic techniques) the nanodevices proposed in the manuscript.

**Funding.** Coordenação de Aperfeiçoamento de Pessoal de Nível Superior (88882.333353/2019-01); Conselho Nacional de Desenvolvimento Científico e Tecnológico (152970/2022-3).

**Acknowledgments.** We gratefully acknowledge the LME-PSI of the Electronic Systems Engineering Department of POLI-USP; the Magnetic Materials Laboratory of the Department of Materials and Mechanics, IF-USP; Cristalography IF-USP, the LabMicro of the Metallurgical and Materials Engineering Department of POLI-USP and the Laboratory of Electroactive Materials of the Fundamental Chemistry Department, IQ-USP.

**Disclosures.** The authors declare no conflicts of interest.

**Data availability.** Data underlying the results presented in this paper are not publicly available at this time but may be obtained from the authors upon reasonable request.

**Supplemental document.** See Supplement 1 for supporting content.

#### References

- A. Ashkin, J. M. Dziedzic, J. E. Bjorkholm, et al., "Observation of a single-beam gradient force optical trap for dielectric particles," Opt. Lett. 11(5), 288–290 (1986).
- A. Ashkin and J. M. Dziedzic, "Optical trapping and manipulation of viruses and bacteria," Science 235(4795), 1517–1520 (1987).
- A. Ashkin, K. Schütze, J. M. Dziedzic, et al., "Force generation of organelle transport measured in vivo by an infrared laser trap," Nature 348(6299), 346–348 (1990).
- T. T. Perkins, D. E. Smith, R. R. G. Larson, et al., "Stretching of a single tethered polymer in a uniform flow," Science 268(5207), 83–87 (1995).
- E. A. Abbondanzieri, W. J. Greenleaf, J. W. Shaevitz, et al., "Direct observation of base-pair stepping by RNA polymerase," Nature 438(7067), 460–465 (2005).
- A. Lisica and S. W. Grill, "Optical tweezers studies of transcription by eukaryotic RNA polymerases," Biomolecular concepts 8(1), 1–11 (2017).

- Y. Arita, M. Mazilu, and K. Dholakia, "Laser-induced rotation and cooling of a trapped microgyroscope in vacuum," Nat. Commun. 4(1), 2374 (2013).
- D. B. Phillips, M. J. Padgett, S. Hanna, et al., "Shape-induced force fields in optical trapping," Nat. Photonics 8(5), 400–405 (2014).
- M. Capitanio, M. Canepari, M. Maffei, et al., "Ultrafast force-clamp spectroscopy of single molecules reveals load dependence of myosin working stroke," Nat. Methods 9(10), 1013–1019 (2012).
- R. Diekmann, D. L. Wolfson, C. Spahn, et al., "Nanoscopy of bacterial cells immobilized by holographic optical tweezers," Nat. Commun. 7(1), 13711 (2016).
- 11. G. Bolognesi, M. S. Friddin, A. Salehi-Reyhani, et al., "Sculpting and fusing biomimetic vesicle networks using optical tweezers," Nat. Commun. 9(1), 1882 (2018).
- 12. L. Novotny, R. X. Bian, and X. S. Xie, "Theory of nanometric optical tweezers," Phys. Rev. Lett. 79(4), 645 (1997).
- O. J. Martin and C. Girard, "Controlling and tuning strong optical field gradients at a local probe microscope tip apex," Appl. Phys. Lett. 70(6), 705–707 (1997).
- Y. Tsuboi, T. Shoji, N. Kitamura, et al., "Optical trapping of quantum dots based on gap-mode-excitation of localized surface plasmon," J. Phys. Chem. Lett. 1(15), 2327–2333 (2010).
- Z. Kang, H. Zhang, H. Lu, et al., "Plasmonic optical trap having very large active volume realized with nano-ring structure," Opt. Lett. 37(10), 1748–1750 (2012).
- S. Zhang, Z. Yong, Y. Shi, et al., "Numerical analysis of an optical nanoscale particles trapping device based on a slotted nanobeam cavity," Sci. Rep. 6(1), 35977 (2016).
- V. Yannopapas and E. Paspalakis, "Electrodynamic multiple-scattering method for the simulation of optical trapping atop periodic metamaterials," J. Mod. Opt. 65(13), 1507–1514 (2018).
- K. Mokri and M. H. Mozaffari, "Numerical design of a plasmonic nano-tweezer for realizing high optical gradient force," Opt. Laser Technol. 119, 105620 (2019).
- P. Alibeigloo, M. Ghorbanzadeh, and M. K. Moravvej-Farshi, "Repositioning of plasmonic hotspots along the sidewalls of conical nanoholes: a numerical investigation," OSA Continuum 3(10), 2817–2829 (2020).
- 20. Y. Pang and R. Gordon, "Optical trapping of a single protein," Nano Lett. 12(1), 402-406 (2012).
- A. A. Saleh and J. A. Dionne, "Toward efficient optical trapping of sub-10-nm particles with coaxial plasmonic apertures," Nano Lett. 12(11), 5581–5586 (2012).
- T. Cao, J. Bao, and L. Mao, "Switching of Giant Lateral Force on Sub-10 nm Particle Using Phase-Change Nanoantenna," Adv. Theory Simulations 1, 1700027 (2018).
- C. Hong, S. Yang, and J. C. Ndukaife, "Stand-off trapping and manipulation of sub-10 nm objects and biomolecules using opto-thermo-electrohydrodynamic tweezers," Nat. Nanotechnol. 15(11), 908-913 (2020).
- 24. J. Zhang, F. Lu, W. Zhang, *et al.*, "Optical trapping of single nano-size particles using a plasmonic nanocavity," J. Phys.: Condens. Matter **32**(47), 475301 (2020).
- 25. C. Zhan, G. Wang, J. Yi, et al., "Single-molecule plasmonic optical trapping," Matter 3(4), 1350–1360 (2020).
- 26. L. Long, J. Chen, H. Yu, *et al.*, "Strong optical force of a molecule enabled by the plasmonic nanogap hot spot in a tip-enhanced Raman spectroscopy system," Photonics Res. **8**(10), 1573–1579 (2020).
- A. A. Khorami, M. K. M. Farshi, and S. Darbari, "Ultralow-power electrically activated lab-on-a-chip plasmonic tweezers," Phys. Rev. Appl. 13(2), 024072 (2020).
- 28. M. Danesh, M. J. Zadeh, T. Zhang, *et al.*, "Monolayer Conveyor for Stably Trapping and Transporting Sub-1 nm Particles," Laser Photonics Rev. **14**, 2000030 (2020).
- K. M. Oliveira, T. A. Moura, J. L. Lucas, et al., "Use of Organic Semiconductors as Handles for Optical Tweezers Experiments: Trapping and Manipulating Polyaniline (PANI) Microparticles," ACS Appl. Polym. Mater. 5(6), 3912–3918 (2023).
- 30. S. Mukherjee, J. Mepperi, P. Sahu, *et al.*, "Single-Molecule Optical Tweezers As a Tool for Delineating the Mechanisms of Protein-Processing Mechanoenzymes," ACS Omega **8**(1), 87–97 (2023).
- 31. A. M. Ghanei, A. Aghili, S. Darbari, et al., "Plasmonic vortices for tunable manipulation of target particles, using arrays of elliptical holes in a gold layer," Sci. Rep. 13(1), 54 (2023).
- 32. Y. Yu, D. Wu, Y. Lou, et al., "Boosting Trapping in Dark Mode and Emission in Bright Mode using a Quad-Nanohole," Adv. Opt. Mater. 11, 2202924 (2023).
- M. Romanelli, R. R. Riso, T. S. Haugland, et al., "Effective Single-Mode Methodology for Strongly Coupled Multimode Molecular-Plasmon Nanosystems," Nano Lett. 23(11), 4938–4946 (2023).
- 34. A. J. Hutt and S. C. Tan, "Drug chirality and its clinical significance," Drugs 52(Supplement 5), 1–12 (1996).
- 35. G. Subramanian, Chiral separation techniques: a practical approach, (John Wiley and Sons, 2008).
- D. S. Bradshaw and D. L. Andrews, "Chiral discrimination in optical trapping and manipulation," New J. Phys. 16(10), 103021 (2014).
- M. Nieto-Vesperinas, "Chiral optical fields: a unified formulation of helicity scattered from particles and dichroism enhancement," Phil. Trans. R. Soc. A. 375(2090), 20160314 (2017).
- 38. L. V. Besteiro, A. Movsesyan, O. Avalos-Ovando, *et al.*, "Local growth mediated by plasmonic hot carriers: chirality from achiral nanocrystals using circularly polarized light," Nano Lett. **21**(24), 10315–10324 (2021).
- J. Ni, S. Liu, G. Hu, et al., "Giant helical dichroism of single chiral nanostructures with photonic orbital angular momentum," ACS Nano 15(2), 2893–2900 (2021).

- L. Ohnoutek, N. H. Cho, A. W. Allen Murphy, et al., "Single nanoparticle chiroptics in a liquid: optical activity in hyper-Rayleigh scattering from Au helicoids," Nano Lett. 20(8), 5792–5798 (2020).
- 41. L. Xu, X. Wang, W. Wang, et al., "Enantiomer-dependent immunological response to chiral nanoparticles," Nature **601**(7893), 366–373 (2022).
- 42. Z. Yuan, Y. Zhou, Z. Qiao, et al., "Stimulated chiral light–matter interactions in biological microlasers," ACS Nano 15(5), 8965–8975 (2021).
- 43. L. Ohnoutek, J. Y. Kim, J. Lu, *et al.*, "Third-harmonic Mie scattering from semiconductor nanohelices," Nat. Photonics **16**(2), 126–133 (2022).
- 44. Y. Zhao, A. A. Saleh, and J. A. Dionne, "Enantioselective optical trapping of chiral nanoparticles with plasmonic tweezers," ACS Photonics 3(3), 304–309 (2016).
- H. Niinomi, T. Sugiyama, A. C. Cheng, et al., "Chiral optical force generated by a superchiral near-field of a plasmonic triangle trimer as origin of giant bias in chiral nucleation: a simulation study," J. Phys. Chem. C 125(11), 6209–6221 (2021).
- L. Fang and J. Wang, "Optical trapping separation of chiral nanoparticles by subwavelength slot waveguides," Phys. Rev. Lett. 127(23), 233902 (2021).
- 47. H. A. A. Champi, R. H. Bustamante, and W. J. Salcedo, "Optical enantioseparation of chiral molecules using asymmetric plasmonic nanoapertures," Opt. Mater. Express 9(4), 1763–1775 (2019).
- P. Librizzi, A. Biswas, R. Chang, et al., "Broadband chiral hybrid plasmon modes on nanofingernail substrates," Nanoscale 12(6), 3827–3833 (2020).
- L. Mao, K. Liu, M. Lian, et al., "Bound States in the Continuum in All-Dielectric Metasurface: Separation of Sub-10 nm Enantiomers," Adv. Photonics Res. 3, 2100280 (2022).
- L. Mao, P. Cheng, K. Liu, et al., "Sieving nanometer enantiomers using bound states in the continuum from the metasurface," Nanoscale Adv. 4(6), 1617–1625 (2022).
- G. Rui, Y. Ji, B. Gu, et al., "Nanoscale chiral imaging under complex optical field excitation with controllable oriented chiral dipole moment," Opt. Express 30(23), 42696–42711 (2022).
- 52. Y. Li, G. Rui, S. Zhou, et al., "Enantioselective optical trapping of chiral nanoparticles using a transverse optical needle field with a transverse spin," Opt. Express 28(19), 27808–27822 (2020).
- 53. T. Horai, H. Eguchi, T. Iida, et al., "Formulation of resonant optical force based on the microscopic structure of chiral molecules," Opt. Express 29(23), 38824–38840 (2021). Science advances 8, eabq2604 (2022).
- 54. H. Yamane, N. Yokoshi, H. Ishihara, *et al.*, "Enantioselective optical trapping of single chiral molecules in the superchiral field vicinity of metal nanostructures," Opt. Express **31**(9), 13708–13723 (2023).
- 55. G. D. Sulka and W. J. Stępniowski, "Structural features of self-organized nanopore arrays formed by anodization of aluminum in oxalic acid at relatively high temperatures," Electrochimica Acta **54**(14), 3683–3691 (2009).
- M. S. Ilango, A. Mutalikdesai, and S. K. Ramasesha, "Anodization of Aluminium using a fast two-step process," J. Chem. Sci. 128(1), 153–158 (2016).
- Z. Wang, Y. K. Su, and H. L. Li, "AFM study of gold nanowire array electrodeposited within anodic aluminum oxide template," Appl. Phys. A 74(4), 563–565 (2002).
- 58. T. Kondo, M. Tanji, K. Nishio, *et al.*, "Cross-Striped Ordered Arrays of Au Nanoparticles in Anodic Porous Alumina Matrix," Electrochem. Solid-State Lett. **9**(12), C189–C191 (2006).
- T. Kondo, K. Nishio, and H. Masuda, "Surface-Enhanced Raman Scattering in Multilayered Au Nanoparticles in Anodic Porous Alumina Matrix," Appl. Phys. Express 2, 032001 (2009).
- 60. S.-H. Gong, A. Stolz, G.-H. Myeong, *et al.*, "Effect of varying pore size of AAO films on refractive index and birefringence measured by prism coupling technique," Opt. Lett. **36**(21), 4272 (2011).
- B. R. Scharifker and J. Mostany, "Three-dimensional nucleation with diffusion controlled growth: Part I. Number density of active sites and nucleation rates per site," J. Efectroanal. Chem. 177(1-2), 13–23 (1984).
- 62. J. Mostany, B. R. Scharifker, K. Saavedra, et al., "Electrochemical nucleation and the classical theory: Overpotential and temperature dependence of the nucleation rate," Russian J. Electrochem. 44(6), 652–658 (2008).
- V. Amendola, R. Pilot, M. Frasconi, et al., "Surface plasmon resonance in gold nanoparticles: a review," J. Phys.: Condens. Matter 29(20), 203002 (2017).
- 64. R. Borah and S. W. Verbruggen, "Coupled plasmon modes in 2D gold nanoparticle clusters and their effect on local temperature control," J. Phys. Chem. C 123(50), 30594–30603 (2019).
- 65. R. Borah, R. Ninakanti, S. Bals, *et al.*, "Plasmon resonance of gold and silver nanoparticle arrays in the Kretschmann (attenuated total reflectance) vs. direct incidence configuration," Sci. Rep. **12**(1), 15738 (2022).
- 66. C. Forestiere, L. Dal-Negro, and G. Miano, "Theory of coupled plasmon modes and Fano-like resonances in subwavelength metal structures," Phys. Rev. B 88(15), 155411 (2013).
- 67. F. Hao, P. Nordlander, Y. Sonnefraud, *et al.*, "Tunability of subradiant dipolar and Fano-type plasmon resonances in metallic ring/disk cavities: implications for nanoscale optical sensing," ACS Nano 3(3), 643–652 (2009).
- J. B. Lassiter, H. Sobhani, J. A. Fan, et al., "Fano resonances in plasmonic nanoclusters: geometrical and chemical tunability." Nano Lett. 10. 3184–3189 (2010).
- K. Thyagarajan, J. Butet, and O. J. Martin, "Augmenting second harmonic generation using Fano resonances in plasmonic systems," Nano Lett. 13(4), 1847–1851 (2013).
- M. Hentschel, M. Saliba, R. Vogelgesang, et al., "Transition from isolated to collective modes in plasmonic oligomers," Nano Lett. 10(7), 2721–2726 (2010).

- B. Hopkins, A. N. Poddubny, A. E. Miroshnichenko, et al., "Revisiting the physics of Fano resonances for nanoparticle oligomers," Phys. Rev. A 88(5), 053819 (2013).
- B. S. Gould, "Amino Acids and Serum Proteins. Advances in Chemistry Series, No. 44," J. Am. Chem. Soc. 87(5), 1152 (1965).
- A. García-Etxarri and J. A. Dionne, "Surface-enhanced circular dichroism spectroscopy mediated by nonchiral nanoantennas," Phys. Rev. B 87(23), 235409 (2013).
- 74. M. Lorente-Crespo, L. Wang, R. Ortu no, *et al.*, "Magnetic hot spots in closely spaced thick gold nanorings," Nano Lett. **13**(6), 2654–2661 (2013).
- 75. R. Verre, Z. J. Yang, T. Shegai, *et al.*, "Optical magnetism and plasmonic Fano resonances in metal–insulator–metal oligomers," Nano Lett. **15**(3), 1952–1958 (2015).
- 76. D. Wu, H. Yu, J. Yao, et al., "Efficient magnetic resonance amplification and near-field enhancement from gain-assisted silicon nanospheres and nanoshells," J. Phys. Chem. C 120(24), 13227–13233 (2016).